Contents lists available at ScienceDirect

# **Energy Storage Materials**

journal homepage: http://ees.elsevier.com



# A three-dimensional interconnected polymer/ceramic composite as a thin film solid electrolyte☆

 $\label{eq:max J. Palmer a} \text{Max J. Palmer a}, \ \text{Sergiy Kalnaus}^{\,b,**}, \ \text{Marm B. Dixit}^{\,c}, \ \text{Andrew S. Westover}^{\,a}, \ \text{Kelsey B. Hatzell}^{\,c},$ Nancy J. Dudney <sup>a</sup>, X. Chelsea Chen <sup>a,\*</sup>

- <sup>a</sup> Chemical Sciences Division, USA
- <sup>b</sup> Computational Science and Engineering Division, Oak Ridge National Laboratory, Oak Ridge, TN, 37830, USA
- <sup>c</sup> Department of Mechanical Engineering, Vanderbilt University, Nashville, TN, USA, 37240

#### ARTICLE INFO

#### Keywords Composite electrolyte Spray coating Ionic conductivity Solid state electrolyte X-ray tomography

#### ABSTRACT

In this work we introduce an approach to fabricate a solid composite electrolyte film that is thin, ionically conductive, and mechanically robust with good potential for manufacturability, for the application of lithium metal batteries. First a doped lithium aluminum titanium phosphate ceramic thin film with thickness of  $\sim\!25~\mu m$  is formed by aqueous spray coating, a scalable process. The film is partially sintered to form a three-dimensionally interconnected structure with a dense backbone. It is then backfilled with a crosslinkable poly(ethylene oxide) (PEO)-based polymer electrolyte. The composite has very high ceramic loading of 77 wt% (61 vol%) and an ionic conductivity of  $3.5 \times 10^{-5}$  S/cm at 20 °C with an activation energy of 0.43 eV. The main ion transport pathway is through the ceramic network, predicted by modelling and verified by experiments. Owing to the interconnected structure of the ceramic, the composite electrolyte exhibits much improved mechanical strength.

# 1. Introduction

Solid electrolytes are promising in enabling lithium metal to replace the conventional graphite anode to significantly increase the capacity and energy density of lithium-ion batteries [1,2]. There are two classes of solid electrolytes, inorganic oxide- or sulfide-based electrolytes and polymer-based electrolytes [3,4]. Inorganic electrolytes offer superb ionic conductivities (10-4-10-2 S/cm) but they suffer from brittleness and lack of processability. Solid polymer electrolytes offer the advantages of flexibility, low-cost processing, and good adhesion to the electrodes, but they typically have low room-temperature ionic conductivity and not sufficient mechanical modulus to stop dendrite growth.

A composite combining inorganic and polymer electrolytes may boast the advantages of each to create a highly conductive, mechanically robust and easily manufacturable solid electrolyte [5]. Most work on composite electrolytes involves dispersing a ceramic filler into the polymer to improve the conductivity and the mechanical strength [6-19]. At low loadings ( < 10 vol%), passive fillers such as SiO $_2$  and Al $_2$ O $_3$  and  $\mathrm{Li}^+$ -conducting active fillers such as  $\mathrm{Li}_{1.3}\mathrm{Al}_{0.3}\mathrm{Ti}_{1.7}(\mathrm{PO}_4)_3$ 

(LATP) [13–15],  $Li_{10}GeP_2S_{12}$  (LGPS) [16],  $Li_7La_3Zr_2O_{12}$  (LLZO) [17], and Li 35La 55TiO3 (LLTO) [18] improve the ionic conductivity of the composite electrolytes. The underlying mechanisms for the conductivity enhancement include suppression of crystallization of the polymer around the filler [20,21], changes in the Li<sup>+</sup> - polymer complexation [19,22], and enhanced surface transport [23]. It is important to note that in these composite systems where discrete particles are dispersed in a polymer matrix, the ceramic's effects lie in enhancing the polymer phase's conductivity. Our recent work revealed a large interfacial resistance for ion transport between the polymer and ceramic electrolytes, which prevented ions to transport across the polymer-ceramic interface in a dispersed composite [24-26].

With higher loadings of ceramic (>50 vol%), which are necessary to achieve the required mechanical modulus [27], composite electrolytes with discrete ceramic fillers show greatly decreased ionic conductivity compared to the neat polymer electrolyte, even with ionically conductive fillers such as LATP and LLZO [24,28]. Although this loading regime is above the ceramic percolation threshold, ion transport through the dispersed ceramic fillers is not efficient due to the large in-

E-mail addresses: kalnauss@ornl.gov (S. Kalnaus); chenx@ornl.gov (X.Chelsea Chen)

<sup>\*</sup> This manuscript has been authored by UT-Battelle, LLC under Contract No. DE-AC05-00OR22725 with the U.S. Department of Energy. The United States Government retains and the publisher, by accepting the article for publication, acknowledges that the United States Government retains a non-exclusive, paid-up, irrevocable, world-wide license to publish or reproduce the published form of this manuscript, or allow others to do so, for United States Government purposes. The Department of Energy will provide public access to these results of federally sponsored research in accordance with the DOE Public Access Plan (http://energy.gov/downloads/doe-public-access-plan).

Corresponding author.

<sup>\*\*</sup> Corresponding author.

terparticle contact resistance and insufficient particle-particle contact area. Therefore, the traditional method of fabricating composites with discrete particles makes it difficult to take advantage of the high ionic conductivity of the ceramic.

In order to overcome this problem, our strategy is to make a composite with an interconnected ceramic network to significantly reduce interparticle resistance [29]. In this work, we demonstrate the development of a composite solid electrolyte with an interconnected ceramic structure using a readily scalable processing method. The composite electrolyte is thin (below 25  $\mu m$ ), has high ceramic volume fraction (ca. 77 wt% and 61 vol%), high room temperature ionic conductivity (3.5  $\times$  10 $^{-5}$  S/cm at 20 °C), and shows good mechanical strength (equibiaxial strength of 19.5 MPa).

#### 2. Experimental section

#### 2.1. Preparation of sintered ceramic thin films and pellets

A 2 wt% aqueous suspension of doped-lithium aluminum titanium phosphate (LICGC<sup>TM</sup>, Ohara Corporation) powders was spray coated onto an alumina substrate at 110 °C using an automatic spraycoater (Prism-400 BT from Ultrasonic Systems, Inc.) The spray nozzle of the automatic spray coater rastered in a programmed area above the heated alumina substrate while the ceramic particles were sprayed out of the nozzle, forming a very thin layer on the substrate. After the spray nozzle completed rastering the defined area once, the film was dried for 1 min. The spraying/drying process was repeated until the desired thickness ( $\sim$ 20  $\mu$ m) was reached. The spray nozzle width, nozzle speed, and flow rate were set at 5 mm, 50 mm/s, and 1 mL min<sup>-1</sup>, respectively. For ceramic pellets, a quarter of a gram of LICGC<sup>TM</sup> powders were cold pressed using a half-inch die with 41 MPa pressure.

Thin film and pellet samples were sintered at 1000 °C for 3 h under dry air to form an interconnected structure. The furnace temperature increased at a ramp rate of 10 °C  $\rm min^{-1}$  and decreased naturally on power off.

# 2.2. Preparation of xPEO polymer electrolyte and filling of the sintered ceramic

O,O'-Bis(2-aminopropyl) polypropylene glycol-block-polyethylene glycol-block-polypropylene glycol (Jeffamine ED-900, Sigma-Aldrich) and poly(ethylene glycol) diglycidyl ether (PEGDGE, average  $M_n$  500, Sigma-Aldrich) were mixed in a weight ratio of 9:10 at room temperature under constant stirring for 2 h. Lithium bis-trifluoromethanesulfonimide (LiTFSI, 3 M) was then added to the mixture and stirred for another 2 h, until it was fully dissolved. The weight ratio of LiTFSI to Jeffamine + PEGDGE was 1:4. The liquid mixture was dispensed onto the sintered ceramic thin film or pellet. To ensure complete filling, the samples were placed in a vacuum oven at room temperature under vacuum for 4 h. Then the polymer mixture was cured at 100 °C under vacuum for 16 h. We denote crosslinked Jeffamine + PEGDGE + LiTFSI polymer electrolyte xPEO. The resulting composite thin films or pellets were then transferred into an argon glovebox and dried further inside the glovebox in a vacuum furnace at 80 °C for 16 h.

# 2.3. X-ray diffraction (XRD)

XRD measurements on LICGC<sup>TM</sup> powder and sintered films/pellets were performed on a Scintag XDS 2000 powder diffractometer with Cu K $\alpha$  radiation ( $\lambda=1.540562$  Å) in the  $2\theta$  range of  $10–90^\circ$ . The operating voltage and current of the X-ray generator were 45 kV and 35 mA, respectively.

#### 2.4. Thermal gravimetric analysis (TGA) measurements

A piece of neat xPEO and a piece of the composite pellet, each containing approximately 7 mg of polymer, were thoroughly dried in the glovebox, following the same procedure as the drying of the composite. Each sample was transferred in an airtight jar to outside the glovebox and loaded onto the TGA immediately after opening the jar. TGA was run in the temperature range of 20 °C–600 °C at a heating rate of 10 °C min $^{-1}$  (TA Instruments Q500). A steady flow of dry nitrogen or dry air at the rate of 10 mL min $^{-1}$  was maintained throughout the measurements. The weight loss results from TGA performed in dry nitrogen and dry air were statistically the same.

#### 2.5. Synchrotron X-ray tomography

A piece of LICGCTM/xPEO composite thin film on substrate was cut into a small matchstick shaped sample with the dimension of 0.5 mm  $\times$  0.5 mm  $\times$  (20  $\mu m$  film + 450  $\mu m$  substrate) using a diamond saw. The sample was mounted on a tomography sample stage using epoxy adhesive. Tomography experiments were carried out at Beamline 2-BM at the Advanced Photon Source. Filtered, monochromatic X-rays with 25 keV energy were used for the experiments. 1500 projections were taken for 180° rotation of sample with 100 ms exposure. The total scan time for sample was  $\sim\!\!4$  min. FLIR Oryx-10GE camera was coupled with a 2X magnification lens resulting in a field of view of  $\sim\!\!2\times1.5$  mm with a resolution of  $\sim\!\!0.7$   $\mu$ m. The tomography reconstructions were carried out using Tomopy software [30]. Subsequent image processing, analysis and visualization was carried out in ImageJ [31] and DragonFly.

#### 2.6. Conductivity modeling

We used a random resistor method to model the partial-sintered LICGC<sup>TM</sup>'s conductivity. The particle size distribution of LICGC<sup>TM</sup> particles is bi-modal, measured by the laser diffraction particle size analysis (LDPSA). The size distribution was modeled by two Weibull distributions and the microstructure was approximated by an assembly of randomly packed spherical particles in a cube with 20  $\mu$ m sides. A 20% overlap between the particles in contact was allowed to approximate the effect of sintering. This microstructure was meshed by a system of resistors, and the effective conductivity was obtained by calculating the total current in the system under an applied potential difference.

#### 2.7. AC Impedance measurements

The impedance spectra of partially sintered LICGC<sup>TM</sup> pellet, fully dense LICGC<sup>TM</sup> plate and LICGC<sup>TM</sup>/xPEO composite pellet were measured by sputtering 500 nm of gold on both sides of the samples. These samples were thoroughly dried in an Ar glovebox following the same procedure described above and sealed in pouch cells before measurement. The impedance spectrum of the as-pressed, unsintered LICGC<sup>TM</sup> pellet was collected by pressing 0.1 g of dried LICGC<sup>TM</sup> powder in a polyether ether ketone (PEEK) die under 41 MPa pressure with the leads to the impedance spectrometer connected to the polished stainless steel pellets. This was done in an argon filled-glovebox.

For composite thin films on alumina substrates, the bottom contact was sputtered onto the alumina substrate prior to spray coating and sintering of the ceramic. The top contact was sputtered after the ceramic network was filled, cured and thoroughly dried. After experimenting with several metals/metal combinations, we discovered that 60 nm of titanium+600 nm of platinum was the best choice as it adhered well to the substrate and remained relatively smooth with-

out degradation or oxidation after heat treatment at 1000  $^{\circ}$ C. The samples were sealed in pouch cells for impedance measurements.

Impedance measurements were carried out by applying an alternating current of  $6\,\text{mV}$  amplitude within a frequency range of  $1\,\text{MHz-}50\,\text{mHz}$  (BioLogic). Samples were equilibrated for  $1.5\,\text{h}$  at each temperature increment before the measurement was taken.

#### 2.8. Mechanical tests

The flexural strength of the composite was measured by equibiaxial deformation in a ring-on-ring setup, according to the ASTM C1499-15 standard. A 3.5 mm thick disk of composite electrolyte material was prepared by the sintering and back-filling procedure described above. The disc was 30 mm in diameter. The flexural strength test was performed in an Instron electromechanical universal testing frame equipped with a 1.33 kN load cell. The biaxial setup consists of a support ring, 22.2 mm in diameter, and the upper loading ring (5.5 mm in diameter) to which the axial load is applied via spherical coupling. All the load bearing parts are made of alumina. To minimize friction, a graphite tape was placed between the loading rings and the sample.

#### 3. Results and discussion

The ceramic we used was a doped-lithium aluminum titanium phosphate (LATP) glass ceramic powder obtained from Ohara corporation (LICGCTM). The average primary particle size was 1  $\mu m$ . Fig. 1 shows the fabrication procedure of the composite electrolyte film. Briefly, an aqueous suspension of ceramic particles was spray coated onto an alumina substrate to form a thin film (~25  $\mu m$  in thickness). Details of the spray coating process are described in the Experimental section. After spray coating, the ceramic thin film was partially sintered to form an interconnected necked structure. Following the sintering step, the film was filled with crosslinkable polymer electrolyte precursors and cured to form a composite electrolyte.

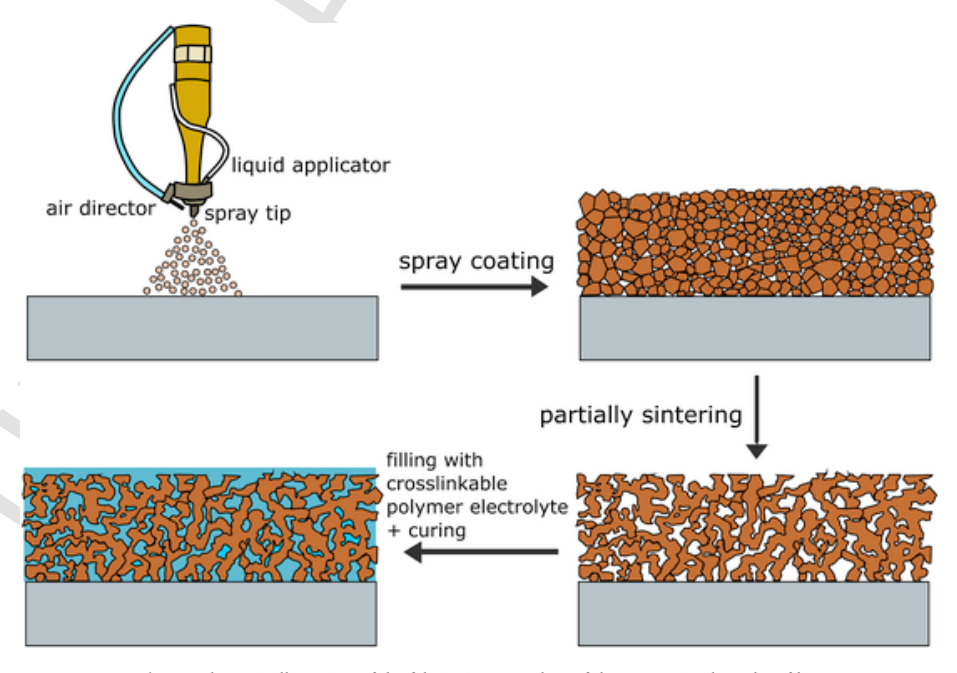
Scanning electron microscopy (SEM) images of the in-plane and cross-sectional view of the as-sprayed ceramic film are shown in Fig. 2a and b. The spray coating method created a ceramic film that had large area and was densely packed. Excellent thickness control and uniformity can also be observed.

After spray coating, the ceramic thin film was sintered at 1000 °C for 3 h under dry air. Fig. 2c and d shows the in-plane and cross-sectional morphology of the sintered film. With this heating procedure, the LICGC<sup>TM</sup> ceramic went through the initial stage of solid-state sintering and formed a necked structure [32]. The cross-sectional view highlighted that this structure permeated throughout the film. X-ray diffraction (XRD) was performed on the partial-sintered LICGC<sup>TM</sup> ceramic (Fig. S1), which confirmed that no structural or crystallinity changes occurred during the sintering process, only morphological changes. Additionally, Fig. 2d revealed that there was negligible change in the film thickness after sintering. As a comparison of the spray-coating method, LICGC<sup>TM</sup> ceramic powder was cold pressed into a 1 mm thick pellet using a half-inch die with 41 MPa pressure and sintered using the same conditions. A very similar necked morphology was observed (Fig. 2e).

The morphology of the partial-sintered LICGCTM thin film was further investigated by synchrotron X-ray microtomography. A slice of the tomogram in the in-plane direction of the film is shown in Fig. 3a. The white region represents the LICGCTM ceramic, which strongly absorbed X-rays. The black region is the X-ray transparent region which is the voids [33]. The binarization clearly revealed the connectivity of the partially sintered ceramic structure. A movie going through all the slices from the top to the bottom surface of the film is shown in the Supporting Information. A volume of 200  $\mu m \times 200~\mu m \times 25~\mu m$  was reconstructed and the ceramic was segmented out as the green component (Fig. 3b). The reconstructed volume indicated that the ceramic network was three-dimensionally interconnected. Furthermore, the binarization indicated that the void area was also interconnected. X-ray tomography confirmed that we successfully created a bicontinuous structure with one phase being the ceramic and another phase being the void to be filled with a polymer electrolyte.

We used a random resistor method to estimate the conductivity of partially-sintered LICGC<sup>TM</sup> [34,35]. The particle size distribution of LICGC<sup>TM</sup> particles is bi-modal, measured by laser diffraction particle size analysis (LDPSA, Fig. 4a). This distribution was modeled by two Weibull distributions. Park and Miller random number generator was used to create a random number following uniform distribution  $U \sim U(0,1)$ , which was then transformed as

$$X = \beta(-\ln(U))^{\frac{1}{\alpha}} \tag{1}$$



 $\textbf{Fig. 1.} \ \ \textbf{Schematic illustration of the fabrication procedure of the composite electrolyte film.}$ 

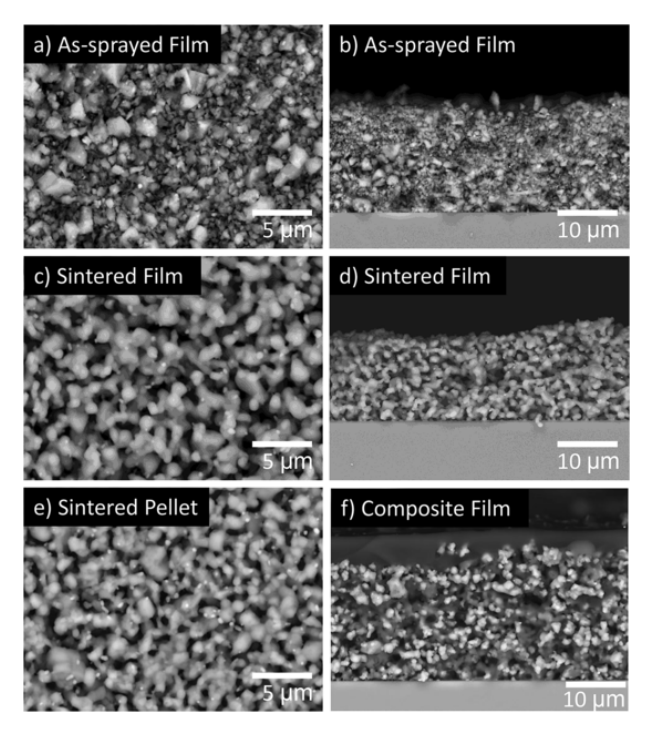


Fig. 2. Scanning electron microscopy (SEM) images of LICGC<sup>TM</sup> thin film ( $\sim$ 20  $\mu$ m thick) and thick pellet ( $\sim$ 1 mm thick). (a), in-plane and (b), cross-section view of as sprayed LICGC<sup>TM</sup> film; (c), in-plane and (d), cross-section view of sintered LICGC<sup>TM</sup> film forming an interconnected necked structure; (e), SEM of sintered LICGC<sup>TM</sup> pellet; (f), cross-section view of the composite film. There is a  $\sim$ 2  $\mu$ m thick polymer-rich layer on the top surface.

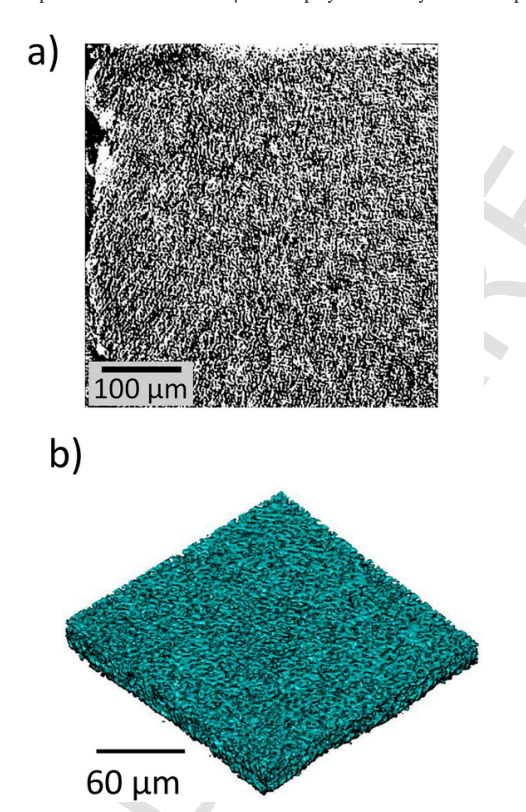


Fig. 3. Synchrotron X-ray microtomography of sintered LICGC™ ceramic thin film. (a), an in-plane slice of the film, where the white region represents LICGC™ ceramic and the black region represents voids; (b), three-dimensional reconstruction of the ceramic thin film. The green segmentation represents LICGC™ ceramic. (For interpretation of the references to color in this figure legend, the reader is referred to the Web version of this article.)

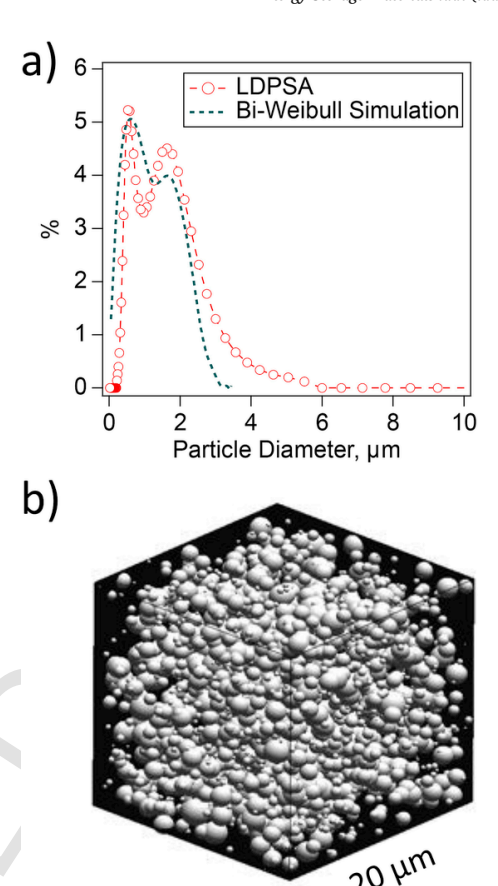


Fig. 4. Modeling of the conductivity of sintered LICGC<sup>TM</sup>. (a), particle size distribution and bi-Weibull simulation; (b), simulation of the microstructure by an assembly of randomly packed spherical particles in a cube with 20  $\mu m$  sides with a 20% overlap between the particles.

where X is the Weibull  $(\alpha,\beta)$  random variable. The resulting distribution was composed of Weibull  $(1.8,\,0.8)$  and Weibull  $(3.8,\,1.94)$  distributions. The result was obtained with 10,000 randomly generated numbers.

The bi-Weibull simulation result is displayed in Fig. 4a. Good agreement with the experimental size distribution was obtained. The microstructure was approximated by an assembly of randomly packed spherical particles in a cube with 20  $\mu m$  sides (Fig. 4b). A 20% overlap between the particles in contact was allowed to approximate the effect of sintering. This microstructure was meshed by a system of resistors, and the effective conductivity was obtained by calculating the total current in the system under an applied potential difference.  $^{14,15}$  Calculations based on 52 vol% particle loading predicted an effective ionic conductivity of 3  $\times$  10 $^{5}$  S/cm at room temperature (23 °C).

After forming the interconnected ceramic network, the thin film and the pellet were filled with a crosslinkable mixture of Jeffamine, PEGDGE and LiTFSI salt [36]. The details of the preparation and filling procedures are described in the Experimental Section. Both Jeffamine and PEGDGE are low viscosity liquids at room temperature and LiTFSI readily dissolves in the mixture. The liquid mixture can easily fill the voids of the ceramic network with the help of vacuum. After filling, the composite film was cured at 100 °C overnight. This promoted the crosslinking of Jeffamine and PEGDGE and the liquid mixture became a solid film with dissolved lithium salt in it. The crosslinked Jaffamine + PEGDGE + LiTFSI polymer electrolyte is hereafter referred to as xPEO. A cross-sectional SEM image of the LICGCTM/xPEO composite thin film is shown in Fig. 2f. There was a  $\sim\!\!2~\mu m$  thick polymer-rich layer on the top surface of the composite film.

To determine the ceramic loading in the composite, thermogravimetric analysis (TGA) was performed on xPEO and LICGCTM/xPEO composite (Fig. S2). The xPEO showed very good thermal stability up to 300 °C. At 600 °C, the remaining weight was approximately 5 wt%. The composite showed similar thermal stability up to 300 °C and the weight loss stopped near 425 °C. From these measurements we calculated remarkably high ceramic loading of 77.4  $\pm$  1.8 wt%, corresponding to 61.1  $\pm$  2.4 vol%. We also measured the density of the sintered LICGCTM pellet by measuring the weight and the volume of several samples. The density of LICGCTM/xPEO composite film was 1.71  $\pm$  0.08 g/cm³. From these measurements, we estimated the volume fraction of the ceramic to be 56.1  $\pm$  2.6%, in good agreement with the TGA results.

The conductivity of as-pressed ceramic pellet, fully dense LICGC<sup>TM</sup> plate, and both thick pellets and thin films of LICGC<sup>TM</sup>/xPEO composite were investigated. The as-pressed ceramic pellet was extremely resistive due to large particle-particle contact resistance. The ionic conductivity was estimated to be between  $10^{-10}$ - $10^{-9}$  S/cm (Fig. S3). The fully dense LICGC<sup>TM</sup> plate's conductivity at 20 °C was  $1.1 \times 10^{-4}$  S/cm. The Nyquist plots of the partially-sintered ceramic-only pellet and the com-

posite pellet at 20 °C are shown in Fig. 5a. The plots were normalized by the thickness and area of the respective samples. The partially-sintered pellet's resistance at 20 °C was  $_{Rsintered\text{-}LICGC}=22~k\Omega$  cm, corresponding to a conductivity of 4.5  $\times$  10  $^{-5}$  S/cm. This is in good agreement with its theoretical conductivity based on volume fraction (vol%  $\sigma_{dense}$  plate = 6.4  $\times$  10  $^{-5}$  S/cm) and model prediction (3  $\times$  10  $^{-5}$  S/cm). This indicates that the ceramic network was well connected, and the backbone of the network was dense.

The LICGC<sup>TM</sup>/xPEO composite pellet had a similar resistance to that of the partially-sintered ceramic,  $R_{\rm composite\ pellet}=29\ {\rm k}\Omega$  cm (Fig. 5a), corresponding to a similar conductivity of  $3.5\times10^{-5}\ {\rm S/cm}$  at  $20\ ^{\circ}{\rm C}$ . These results are very exciting as they revealed that in the LICGC<sup>TM</sup>/xPEO composite, the ion transport mainly went through the ceramic network. This transport mechanism is the opposite of the majority of reports on composite electrolytes with dispersed ceramic fillers where ion transport occurs in the polymer phase [13–18,24,28].

As a comparison, a composite made of xPEO with 70 wt% unsintered and dispersed LICGC $^{\text{TM}}$  ceramic particles, a similar loading to the interconnected composite, was formed through traditional mixing and casting methods. The dispersed composite had an ionic conductivity

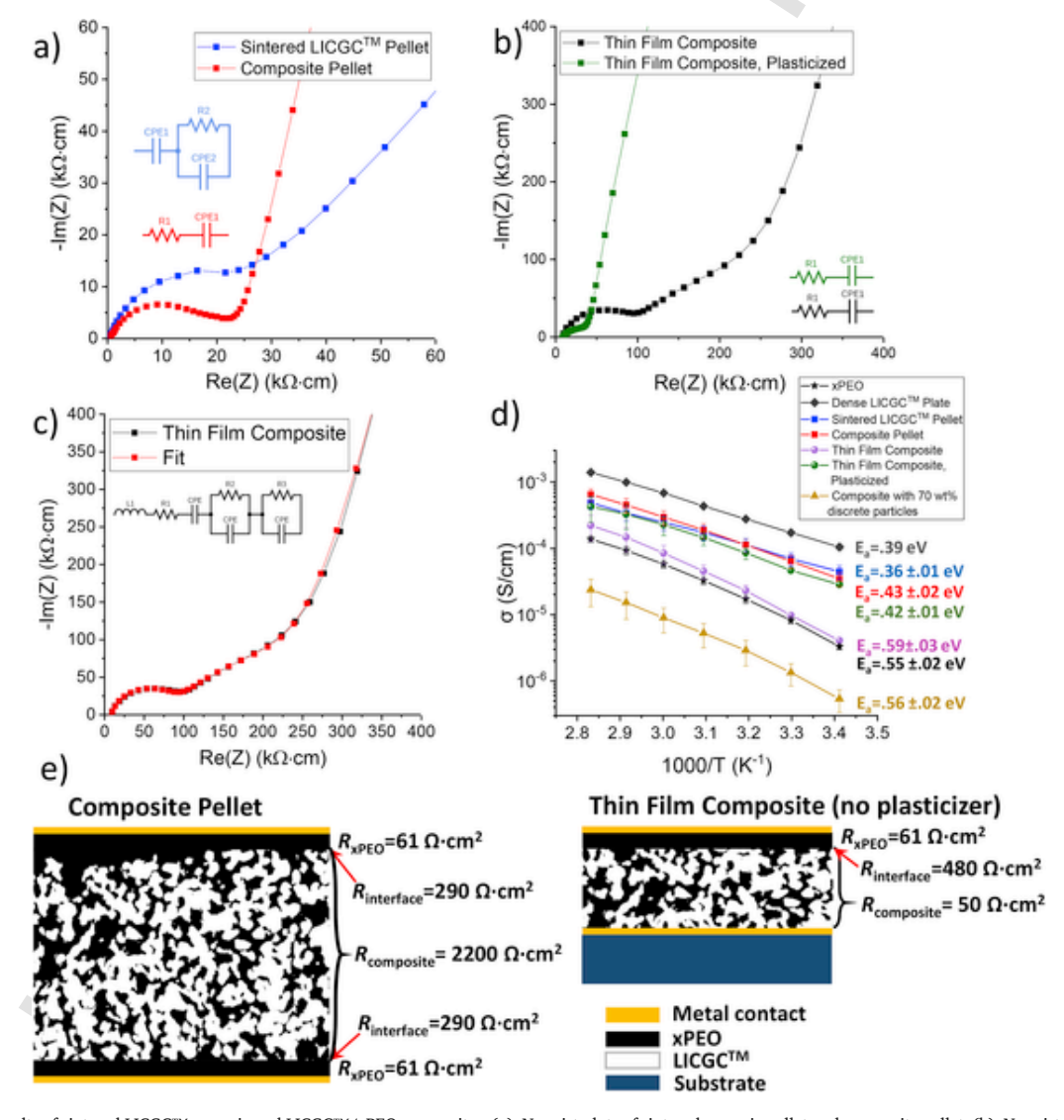


Fig. 5. Impedance results of sintered LICGC™ ceramic and LICGC™/xPEO composites. (a), Nyquist plots of sintered ceramic pellet and composite pellet; (b), Nyquist plots of the composite thin film, and plasticized composite thin film. All the Nyquist plots were collected at 20 °C and normalized by the thickness and area of respective samples. Equivalent circuit models used to extrapolate resistances are color matched with each Nyquist plot. (c), equivalent circuit model and fitting result of the composite thin film. (d), Arrhenius plot of the ionic conductivity of all samples. (e), schematics of the composite pellet and thin film, showing that the effects of surface xPEO layer and interfacial resistance are much larger in the thin film than the thick pellet. Schematics are not drawn to scale. (For interpretation of the references to color in this figure legend, the reader is referred to the Web version of this article.)

of  $5.4 \times 10^{-7}$  S/cm at 20 °C, two orders of magnitude lower than the composite with interconnected ceramic structure (Fig. 5d).

The Nyquist plot of LICGC<sup>TM</sup>/xPEO composite thin film at 20 °C is shown in Fig. 5b. At 20 °C, the thin film composite has a resistance of  $R_{\rm composite-TF}=250~{\rm k}\Omega$  cm, corresponding to an ionic conductivity of  $4.1\times10^{-6}$  S/cm, nearly an order of a magnitude lower than the that of the thick composite pellet. Careful analysis of the impedance spectra revealed the reasons behind the thin film's low ionic conductivity.

In Fig. 5e, we compare the resistance of every layer in the composite pellet and thin film. The composite pellet consists of two xPEO surface layers, a bulk composite layer and two xPEO/composite interfaces. A 2 µm xPEO surface layer has an area specific resistance of  $R_{\text{xPEO}} = 61 \,\Omega \,\text{cm}^2$ , calculated from the conductivity of xPEO. The 1 mm thick composite had an area specific resistance of  $R_{compos}$  $_{\rm ite}$  = 2200  $\Omega$  cm<sup>2</sup>, calculated using the conductivity of the partially-sintered ceramic and assuming the majority of ion conduction went through the ceramic phase. Since the total area specific resistance of the composite pellet was  $R_{\text{composite pellet}} = 2900 \,\Omega \,\text{cm}^2$ , we obtained the interfacial resistance between the surface xPEO layer and the composite bulk layer to be  $R_{\text{interface}} = 290 \,\Omega \text{ cm}^2$ . The interfacial resistance was not clearly observed in the impedance spectrum of the composite pellet at 20 °C, but it became more obvious at higher temperatures, manifesting as an extra semicircle (Fig. S4). In the composite pellet, the surface xPEO layer's resistance and the interfacial resistance summed up to 32% of the composite layer. The origin of this interfacial resistance has been examined in several reports [25,26,37].

Similarly, in the thin film composite, the surface layer has an  $R_{\rm xPEO} = 61 \ \Omega \ {\rm cm}^2$ . Note that there is only one surface xPEO layer in the thin film composite since the thin film had only one free surface. The composite layer had a low area specific resistance of  $R_{\text{compos}}$ - $_{\rm ite} = 50 \,\Omega \,{\rm cm}^2$ , owing to its thinness (Fig. 5e), calculated in the same way as the pellet. Since the whole thin film composite's area specific resistance was  $R_{\text{composite-TF}} = 590 \,\Omega \,\text{cm}^2$ , we obtained an interfacial resistance of  $R_{\text{interface}} = 480 \,\Omega \,\text{cm}^2$ . This is remarkably consistent with the pellet given the assumptions and subtraction of larger values to obtain them. In Fig. 5c we used an equivalent circuit model that includes an interface component (a second RC element) and obtained good fits of the Nyquist plot. In the thin film composite, the surface xPEO layer's resistance and the interfacial resistance summed up to be 1100% of the composite layer, causing a whole order of magnitude decrease in the thin film's conductivity. These results highlight an important fact: when making a composite electrolyte in a commercially relevant form factor, the surface layer and the interface cannot be ignored.

To demonstrate the thin film composite reaches a higher ionic conductivity with an improved interface, tetraethylene glycol dimethyl ether (TEGDME) was added as a plasticizer. The plasticized thin film composite showed an enhanced ionic conductivity of  $2.8 \times 10^{-5}$  S/cm, approaching the conductivity of the composite pellet. The Nyquist plot suggested decrease of the surface xPEO layer's resistance (decrease of the first semicircle) as well as significantly reduced interfacial resistance (disappearance of the second semicircle, Fig. 5b).

Fig. 5d shows Arrhenius plots of the ionic conductivity of all the samples discussed. In the entire measured temperature range (20 °C–90 °C), the partial-sintered LICGC<sup>TM</sup> pellet showed approximately 40% of the ionic conductivity of the densely sintered plate. The activation energy of the partial sintered pellet was 0.36 eV, very similar to that of the dense plate of 0.39 eV, indicating similar ion transport mechanism. The composite pellet had similar ionic conductivity to the partially-sintered pellet across the measured temperature range (20–80 °C), with a slightly higher activation energy of 0.43 eV, likely due to the surface layer and interfacial resistance. The composite pellet had an order of magnitude higher ionic conductivity than neat xPEO.

The thin film composite showed nearly an order of magnitude lower ionic conductivity at low temperature (20–30 °C) and 4–5 fold

lower ionic conductivity at higher temperatures (40–90 °C), compared to the composite pellet. The activation energy of the thin film composite was  $E_{\rm a}=0.59$  eV, higher than that of the pellet (0.43 eV), which is another evidence that the interfacial resistance dominates the ion transport process in the thin film. When plasticized with TEGDME, both the ionic conductivity and the activation energy of the thin film composite were similar to the composite pellet.

As mentioned earlier, traditional composites with discrete ceramic fillers at high ceramic loadings have a decreased ionic conductivity compared to the neat polymer. The composite made of xPEO with 70 wt% unsintered and dispersed LICGC $^{\text{TM}}$  ceramic particles showed two orders of magnitude lower ionic conductivity than the interconnected composite pellet and one order of magnitude lower ionic conductivity than neat xPEO over the entire measured temperature range.

The flexural strength of the composite was measured by equibiaxial deformation in a ring-on-ring setup, according to the ASTM C1499-15 standard [38]. The biaxial setup is shown in Fig. 6. It consists of a support ring, 22.2 mm in diameter, and an upper loading ring (5.5 mm in diameter) to which the axial load is applied via spherical coupling (Fig. 6a and b). The load-displacement curve is shown in Fig. 6c. Interestingly, the load did not drop immediately upon failure, but rather decreased over several steps indicating crack extension in the material. This indicates that polymer back-filling of the ceramic structure provides enough cohesion to support some load until the final fracture in the sample.

Loading was performed in displacement control at 0.012 mm/s which corresponds to the target stress rate of 50 MPa. The experiment was performed at room temperature and in ambient air. The equibiaxial flexure strength was calculated using the formula

$$\sigma_f = \frac{3P}{2\pi h^2} \left[ (1 - \nu) \frac{D_S^2 - D_L^2}{2D^2} + (1 + \nu) \ln \left( \frac{D_S}{D_L} \right) \right]$$
 (2)

where P is the maximum load, h is the sample thickness,  $D_S$  and  $D_L$  are the diameter of supporting and loading rings respectively, and  $\nu$  is the Poisson's ratio, assumed here as equal to 0.25. The resulting equibiaxial strength was calculated to be 19.5 MPa. The failure pattern in Fig. 6d showed no evidence of cracking starting from the edge. Therefore, we consider this a valid test, and the value can be used as an estimate of the composite's equibiaxial strength. The biaxial flexural strength of dense LATP reported in Ref 39 ranges from 49 MPa to 120 MPa, depending on the grain size [39]. Our value (19.5 MPa) is obviously lower, but the most important feature is that our composite membrane is capable of supporting some load after the fracture initiated due to cohesion provided by xPEO. This test is not suitable for low strength polymers such as xPEO. The composite electrolyte with the 3D ceramic network exhibited significantly increased mechanical strength compared to neat xPEO and the polymer phase decreased the brittleness of the composite.

## 4. Conclusions

In summary, we developed a thin solid composite electrolyte with a 3-dimensionally connected structure through a scalable process. We used a simple three step procedure of spray coating a ceramic thin film under 25  $\mu m$  thick, sintering to achieve a necked morphology, and backfilling the ceramic with a polymer to create the composite. The sintered ceramic formed a three dimensional, fully connected structure with necking particles. The filled composite had an exceptionally high LICGCTM loading near 77 wt% and gives a predictable ionic conductivity of 3.5  $\times$  10 $^{-5}$  S/cm at 20 °C, an order of magnitude larger than xPEO and about two orders of magnitude larger than randomly dispersed LICGCTM particles in xPEO near the same loading.

We are currently applying similar processing methods to LLZO ceramic, which has higher conductivity than LATP and is stable with

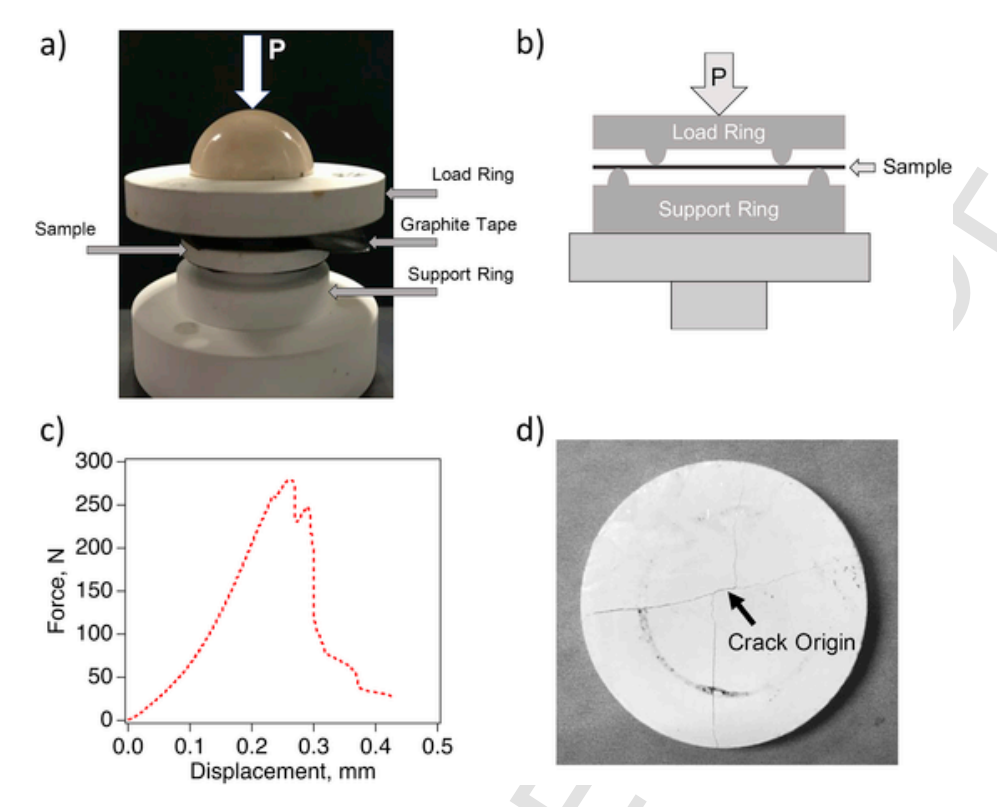


Fig. 6. Equibiaxial flexural strength measurement of the partially-sintered LICGCTM/xPEO composite electrolyte. (a), photo of the loading fixture, (b), schematics showing the load applied to the sample, (c), load-displacement curve, (d), fracture pattern.

Li. Our preliminary data indicate that our method of creating an interconnected ceramic structure is not limited to LATP type ceramics. While sulfide-polymer composites are largely unexplored, sulfides would clearly boost the ionic conductivity and drastically lower the sintering conditions. Additionally, optimize the chemistry of the polymer phase would help improve the stability with lithium metal and lower interfacial resistance [40]. These strategies will be explored in follow-up work. Overall, this process and concept of utilizing an interconnected ceramic backbone for a solid electrolyte can offer a practical class of composites.

#### CRediT authorship contribution statement

Max J. Palmer: Data curation, Methodology, Writing - original draft, Writing - review & editing. Sergiy Kalnaus: Conceptualization, Data curation, Writing - review & editing, Funding acquisition. Marm B. Dixit: Data curation, Formal analysis. Andrew S. Westover: Methodology, Writing - review & editing. Kelsey B. Hatzell: Data curation, Formal analysis. Nancy J. Dudney: Funding acquisition, Project administration, Supervision. X. Chelsea Chen: Conceptualization, Data curation, Methodology, Writing - original draft, Writing - review & editing, Project administration, Supervision.

## Declaration of competing interest

The authors declare that they have no known competing financial interests or personal relationships that could have appeared to influence the work reported in this paper.

#### Acknowledgments

This research at Oak Ridge National Laboratory, managed by UT Battelle, LLC, for the U.S. Department of Energy (DOE), under contract DE-AC05-000R22725, was primarily sponsored by the Office of Energy Efficiency and Renewable Energy for the Vehicle Technologies Office's Ad-

vanced Battery Materials Research program and partially sponsored by the Laboratory Directed Research and Development Program (LDRD) of ORNL. KBH and MD were supported by the National Science Foundation under grant No. 1847029 and the ECS Toyota Fellowship. This research used resources of the Advanced Photon Source, a U.S. Department of Energy (DOE) Office of Science User Facility operated for the DOE Office of Science by Argonne National Laboratory under Contract No. DE-ACO2-06CH11357. We thank Dr. Tomonori Saito and Michelle Lehmann for their help with the polymer electrolytes and Dr. Christopher Nelson for help with the preparation of X-ray tomography samples.

### Appendix A. Supplementary data

Supplementary data to this article can be found online at https://doi.org/10.1016/j.ensm.2019.12.031.

#### References

- [1] P. Albertus, S. Babinec, S. Litzelman, A. Newman, Nat. Energy 3 (2018) 16-21.
- [2] W. Xu, J. Wang, F. Ding, X. Chen, E. Nasybulin, Y. Zhang, J.-G. Zhang, Energy Environ. Sci. 7 (2014) 513–537.
- [3] N.J. Dudney, W.C. West, J. Nanda, Handbook of Solid State Batteries, World Scientific, 2015.
- [4] F. Gray, M. Armand, Polymer electrolytes, in: C. Daniel, J.O. Besenhard (Eds.), Handbook of Battery Materials, Wiley-VCH Verlag & Co. KGaA, Weinheim, Germany, 2011.
- [5] M. Keller, A. Varzi, S. Passerini, J. Power Sources 392 (2018) 206-225.
- [6] F. Croce, G.B. Appetecchi, L. Persi, B. Scrosati, Nature 394 (1998) 456-458.
- [7] I. Villaluenga, X.C. Chen, D. Devaux, D.T. Hallinan, N.P. Balsara, Macromolecules 48 (2015) 358–364.
- [8] W. Wang, E. Yi, A.J. Fici, R.M. Laine, J. Kieffer, J. Phys. Chem. C 121 (2017) 2563–2573.
- [9] M.R. Johan, O.H. Shy, S. Ibrahim, S.M. Mohd Yassin, T.Y. Hui, Solid State Ion. 196 (2011) 41–47.
- [10] D. Lin, W. Liu, Y. Liu, H.R. Lee, P.-C. Hsu, K. Liu, Y. Cui, Nano Lett. 16 (2016) 459–465.
- [11] Y. Tominaga, K. Yamazaki, Chem. Commun. 50 (2014) 4448-4450.
- [12] N. Lago, O. Garcia-Calvo, J.M. Lopez del Amo, T. Rojo, M. Armand, Chem-SusChem 8 (2015) 3039–3043.
- [13] J. Płcharski, W. Weiczorek, Solid State Ion. 28-30 (1988) 979-982.

- [14] S. Xuefu, H. Nemori, S. Mitsuoka, P. Xu, M. Matsui, Y. Takeda, O. Yamamoto, N. Imanishi, Front. Energy Res. 4 (2016).
- [15] L. Yang, Z. Wang, Y. Feng, R. Tan, Y. Zuo, R. Gao, Y. Zhao, L. Han, Z. Wang, F. Pan, Adv. Energy Mater. 7 (2017) 1701437.
- [16] B. Chen, Z. Huang, X. Chen, Y. Zhao, Q. Xu, P. Long, S. Chen, X. Xu, Electrochim. Acta 210 (2016) 905–914.
- [17] J. Zheng, M. Tang, Y.Y. Hu, Angew Chem. Ger. Ed. 128 (2016) 12726–12730.
- [18] L. Chen, Y.T. Li, S.P. Li, L.Z. Fan, C.W. Nan, J.B. Goodenough, Nano Energy 46 (2018) 176–184.
- [19] X. Zhang, T. Liu, S. Zhang, X. Huang, B. Xu, Y. Lin, B. Xu, L. Li, C.-W. Nan, Y. Shen, J. Am. Chem. Soc. 139 (2017) 13779–13785.
- [20] F. Croce, S. Sacchetti, B. Scrosati, J. Power Sources 161 (2006) 560–564.
- [21] Y. Zhao, Z. Huang, S. Chen, B. Chen, J. Yang, Q. Zhang, F. Ding, Y. Chen, X. Xu, Solid State Ion. 295 (2016) 65–71.
- [22] F. Croce, L. Persi, B. Scrosati, F. Serraino-Fiory, E. Plichta, M.A. Hendrickson, Electrochim. Acta 46 (2001) 2457–2461.
- [23] W. Liu, N. Liu, J. Sun, P.-C. Hsu, Y. Li, H.-W. Lee, Y. Cui, Nano Lett. 15 (2015) 2740–2745.
- [24] A.S. Pandian, X.C. Chen, J. Chen, B.S. Lokitz, R.E. Ruther, G. Yang, K. Lou, J. Nanda, F.M. Delnick, N.J. Dudney, J. Power Sources 390 (2018) 153–164.
- [25] X.C. Chen, X. Liu, A.S. Pandian, K. Lou, F.M. Delnick, N.J. Dudney, ACS Energy Lett. 4 (2019) 1080–1085.
- [26] X.C. Chen, R.L. Sacci, N.C. Osti, M. Tyagi, Y. Wang, M.J. Palmer, N.J. Dudney, Mol. Syst. Des. Eng. 4 (2019) 379–385.

- [27] S. Kalnaus, A.S. Sabau, W.E. Tenhaeff, N.J. Dudney, C. Daniel, J. Power Sources 201 (2012) 280–287.
- [28] L. Chen, Y. Li, S.-P. Li, L.-Z. Fan, C.-W. Nan, J.B. Goodenough, Nano Energy 46 (2018) 176–184.
- [29] S. Kalnaus, W.E. Tenhaeff, J. Sakamoto, A.S. Sabau, C. Daniel, N.J. Dudney, J. Power Sources 241 (2013) 178–185.
- [30] D. Gursoy, F. De Carlo, X. Xiao, C. Jacobsen, J. Synchrotron Radiat. 21 (2014) 1188–1193.
- [31] C.A. Schneider, W.S. Rasband, K.W. Eliceiri, Nat. Methods 9 (2012) 671-675.
- [32] R.M. German, Sintering Theory and Practice, Wiley-VCH, 1996.
- [33] F. Shen, M.B. Dixit, X. Xiao, K.B. Hatzell, ACS Energy Lett. 3 (2018) 1056–1061.
- [34] K. Nadara, M. Siekierski, Solid State Ion. 176 (2005) 1781-1786.
- [35] S. Kalnaus, A.S. Sabau, S. Newman, W.E. Tenhaeff, C. Daniel, N.J. Dudney, Solid State Ion. 199–200 (2011) 44–53.
- [36] M.L. Lehmann, G. Yang, D. Gilmer, K.S. Han, E.C. Self, R.E. Ruther, S. Ge, B. Li, V. Murugesan, A.P. Sokolov, F.M. Delnick, J. Nanda, T. Saito, Energy Storage Mater. 21 (2019) 85–96.
- [37] A. Mehrotra, P.N. Ross, V. Srinivasan, J. Electrochem. Soc. 161 (2014) A1681–A1690.
- [38] A. International, in.
- [39] S.D. Jackman, R.A. Cutler, J. Power Sources 218 (2012) 65–72.
- [40] M. Du, K. Liao, Q. Lu, Z. Shao, Energy Environ. Sci. 12 (2019) 1780-1804.